CrystEngComm

Accepted Manuscript

ROYAL SOCIETY OF CHEMISTRY

www.rsc.org/crystengcomm

Journal Name

ARTICLE

Unravelling the mechanism of lithium insertion into and extraction from trirutile-type $LiNiFeF_6$ cathode material for Li-ion batteries

Received 00th January 20xx,
Accepted 00th January 20xx

DOI: 10.1039/x0xx00000x

www.rsc.org/

L. de Biasi[a,b], G. Lieser[a], J. Rana[c], S. Indris[a,b], C. Dräger[a], S. Glatthaar[a], R. Mönig[a,b], H. Ehrenberg[a,b], G. Schumacher[c], J. R. Binder[a], H. Geßwein[a,b]

$LiNiFeF_6$ was used as cathode material in lithium-ion cells and studied by *in situ* X-ray diffraction (XRD), *in operando* X-ray absorption spectroscopy (XAS) and ^{7}Li MAS NMR spectroscopy. An optimised electrochemical *in situ* cell was employed for the structural and electrochemical characterisation of $LiNiFeF_6$ upon galvanostatic cycling. The results for the first time reveal the lithium insertion process into a quaternary lithium transition metal fluoride with a trirutil-type host structure (space group $P4_2/mnm$). The *in situ* diffraction experiments indicate a preservation of the structure type after repeated lithium insertion and extraction. The lithium insertion reaction can be attributed to a phase separation mechanism between Li-poor $Li_{1+x1}NiFeF_6$ and Li-rich $Li_{1+x2}NiFeF_6$ ($x1 \lesssim 0.16 \lesssim x2$), where not only the weight fractions, but also the lattice parameters of the reacting phases change. The insertion of Li ions into [001]-channels of the trirutile structure causes an anisotropic lattice expansion along the tetragonal *a*-axes. An overall increase in the unit cell volume of ~ 6 % and a reduction in the *c/a* ratio of ~ 4 % are detected during discharge. Changes of atomic coordinates and distances suggest the accommodation of intercalated lithium in the empty six-fold coordinated 4c site. This is confirmed by ^{7}Li MAS NMR spectroscopy showing two Li environments with similar intensities after discharging to 2.0 V. Furthermore, *in operando* XAS investigations revealed that only Fe^{3+} cations participate in the electrochemical process via an Fe^{3+}/Fe^{2+} redox reaction, while Ni^{2+} cations remain electrochemically inactive.

1. Introduction

As an alternative to the widely used lithium metal oxides[1,2], lithium transition metal fluorides are studied for cathode applications in lithium-ion batteries for several reasons. Besides a predicted high voltage and energy density due to the high electronegativity of fluorine atoms[3-5], fluoride-based electrode materials exhibit a sufficiently high lithium ion conductivity. This is an important factor for insertion kinetics and a necessary requirement for the use as electrode material. An ionic conductivity of 2×10^{-4} and 6×10^{-5} S cm^{-1} at 300 °C has been reported for Li_2TiF_6 and Li_3AlF_6[6], respectively. Extrapolation of the data to room temperature conditions yields values which reach the order of magnitude of commercially established $LiFePO_4$ cathode material (10^{-9} S cm^{-1})[7]. Although the use of fluorides as cathode material is limited by their low electronic conductivity, it is possible to achieve an adequate electrochemical performance by subjecting a carbon metal fluoride nano composite to high-energy ball milling[8-10].

In situ X-ray powder diffraction is a powerful method in battery research. Structural changes of the active cathode or anode materials, such as phase transitions, the formation of different crystallographic phases, and changes in the atomic arrangement within the unit cell, can be monitored. The complexity of latest Li-ion battery systems often requires the application of synchrotron radiation, because synchrotron sources offer tunable high-energy X-ray radiation. This radiation is needed to penetrate the whole electrochemical *in situ* cell. In addition, a low beam divergence is required for a high angular resolution in order to monitor subtle changes in the diffraction pattern. A recent review of a state-of-the-art synchrotron beamline for Li-ion battery research and a description of an application to high-voltage spinels are given by Herklotz et al.[11] and Yavuz et al.[12], respectively. However, these *in situ* diffraction experiments are often time consuming, the beam time available at synchrotron radiation sources is limited, and in some cases, it is applied too fast to reach the equilibrium.

In this study, it is reported about the investigation of quaternary lithium fluoride $LiNiFeF_6$ during electrochemical cycling under operating conditions. For the detailed examination of the structural changes, a dedicated laboratory X-ray diffraction set-up is combined with an electrochemical cell optimised for *in situ* diffraction of electrode materials with a time resolution of a few minutes. A model for Li insertion is suggested and verified by ^{7}Li NMR spectroscopic measurements. As a complementary technique, X-ray absorption spectroscopy is used to track the changes of the

[a] Institute for Applied Materials, Karlsruhe Institute of Technology (KIT), Hermann-von-Helmholtz-Platz 1, 76344 Eggenstein-Leopoldshafen, Germany.
[b] Helmholtz Institute Ulm (HIU), Helmholtzstraße 11, 89081 Ulm, Germany
[c] Helmholtz-Zentrum Berlin für Materialien und Energie, Hahn-Meitner-Platz 1, 14109 Berlin, Germany.
† Corresponding author. E-mail adress: holger.gesswein@kit.edu (H. Geßwein).

oxidation state and the local environment of the transition metals in the trirutile host structure. While previous work focussed on structural and electrochemical characterisation of various binary metal fluorides[13] and ternary[9,10,14-19] and quaternary[20-23] lithium metal fluorides, the crystal structure of most of these materials still remains to be investigated under operating conditions of a battery.

Recently, the synthesis of $LiNiFeF_6$ by the usage of a non-hazardous sol-gel process was reported[20]. For the first time, a quaternary lithium transition metal fluoride with two different transition metals was successfully used as a positive electrode in a Li-ion battery and analysed for its electrochemical properties. Based on X-ray diffraction measurements, the structure of the $LiNiFeF_6$ active material was identified to be of a partly ordered trirutile type (space group $P4_2/mnm$). During cycling, a discharge capacity of 95 mAh g^{-1} could be achieved, which corresponds to 84 % of the theoretical capacity based on the insertion of 1 Li per formula unit. The cycle stability test yielded 93 % of the initial capacity after 20 cycles and, hence, confirmed stability of the host structure during Li insertion. Insertion into oxide-based rutile TiO_2 is known to be possible without destruction of the host structure[24]. However, the structure-related dirutile and rutile fluoride $LiMnF_4$ (space group $P2_1/c$) was reported to be converted into LiF, MnF_2, and α-Mn upon lithiation[17]. *Ex situ* X-ray diffraction analysis of trirutile Li_2TiF_6[14] and $LiNiFeF_6$[20] suggests a preservation of the trirutile structure and an insertion mechanism similar to isostructural $LiFeFeF_6$[21]. Liao et al.[21] investigated the electrochemical properties and the insertion mechanism of the disordered trirutile-type transition metal fluoride $LiFeFeF_6$. They suggested that lithium ions can be inserted and extracted through the [001]-oriented channels and cation chains, although no model was published for the evolution of lattice parameters or the atomic structure. Knowledge of the structural changes of quaternary lithium transition metal fluorides of trirutile structure will help understand their lithium (de-)insertion mechanisms under operating conditions. Here, we present *in situ* XRD, ^{7}Li NMR, and *in operando* XANES results showing, for the first time, the reversible lithium insertion mechanism into the trirutile-type $LiNiFeF_6$.

2. Experimental

The synthesis of the $LiNiFeF_6$ active material as well as the preparation of cathodes was realised as described in a former report[20]. After drying, the cathodes of 12 mm in diameter were assembled into an *in situ* cell under argon atmosphere in a glove box. For this study, crimped coin cell type batteries optimised for *in situ* investigations were used. The cells are designed for measurements in the transmission mode, which is particularly suitable for the investigation of lithium insertion processes, since the complete volume of the electrode contributes to scattering. In reflection geometry, by contrast, only the near-surface region is probed by the X-rays which may not reflect the behaviour of the bulk electrode material[25]. The thickness of the cell components was chosen to achieve a feasible compromise between cell stability/operational reliability and maintaining a tolerable X-ray absorption. As the negative counter electrode, lithium foil was fixed to a steel current collector. The highly absorbing steel current collector was provided with a hole in the centre for the beam to pass. The cell was additionally equipped with one sheet of Whatman GF/C glass micro fibre separator. A solution of $LiPF_6$ (1 M) in ethylene carbonate (EC) and dimethyl carbonate (DMC) [1:1] was used as the electrolyte. The coin cells were sealed in the glove box by crimping. An insulating PE ring was used for separating the two parts of the steel housing to prevent shorting and ensure appropriate sealing by preventing electrolyte evaporation.

2.1. *In situ* X-ray diffraction

The *in situ* X-ray powder diffraction experiments were performed in a home-built laboratory diffractometer dedicated to battery research. The diffractometer is equipped with a molybdenum micro focus rotating anode generator (Rigaku MM-007 HF) and a 2D collimating Osmic VariMax multilayer optical system. A parallel beam (divergence < 0.3 mrad) with a photon flux of the order of 10^8 photons per second can be achieved. The optional Ge (111) channel cut monochromator for pure Mo-Kα_1 radiation was used solely for the additional *ex situ* experiments in order to expose the *in situ* sample to the maximum possible photon flux. The *in situ* cell was held by a sample holder in the centre of the goniometer and electrically connected to an Ivium CompactStat potentiostat for simultaneous electrochemical data acquisition. Using a slit system manufactured by JJ X-ray, the beam dimensions were adjusted to obtain an illuminated sample area of 0.6 mm in height and 1.7 mm in width.

The cathode containing 14.9 mg of $LiNiFeF_6$ active material was cycled against the lithium metal anode under galvanostatic conditions with a current density of 5.33 mA g^{-1} (~C/20). Parallel to electrochemical cycling, two-dimensional XRD patterns were acquired in Debye-Scherrer transmission geometry with a Pilatus 300K-W area detector having an exposure time of 300 sec. The intensities of two consecutive diffraction images were added for further evaluation, resulting in a time resolution of 10 min. Calibration of the detector geometry and integration of two-dimensional X-ray diffraction images to one-dimensional diffraction patterns were performed using the software package XRDUA[26].

Rietveld refinement of the structure model was performed with the software TOPAS version 4.2 (Bruker AXS). The instrumental resolution function was determined with an annealed CeO_2 sample and was described with a pseudo-Voigt profile function of Thompson, Cox, and Hastings[27]. Sample broadening effects of the synthesised materials, such as the apparent crystallite size and micro strain, were accounted for using convolution-based profile fitting as implemented in the TOPAS programme. This approach is equivalent to the Double-Voigt method as described by Balzar[28] and is based on the integral breadths of the diffraction lines. The micro strain calculated with TOPAS corresponds to an apparent maximum upper-limit strain given by $\varepsilon = \Delta d/d = \beta_D(2\theta)/4\tan(\theta)$,

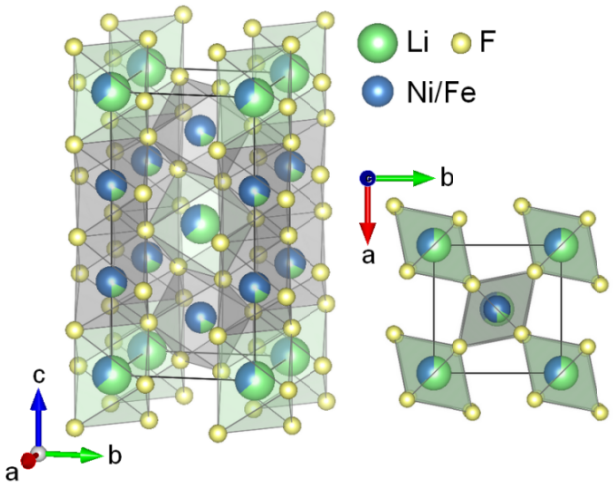

Figure 1. Crystal structure of the ball-milled $LiNiFeF_6$ active material (a) perpendicular to c-axis and (b) along c-axis.

where β_D is the distortion related-integral breadth[29]. A zero-point correction defined by Norby[30] was used to correct possible sample displacement errors of the active material and Al current collector. The background refinement was made using a 14-term Chebyshev polynomial background function. Graphical images of the structure were designed with the VESTA software package[31].

During the refinements, the weight fractions of the individual phases as well as the lattice parameters and strain parameters were allowed to vary, whereas the atomic coordinates of the crystal structures were fixed. The crystal structure data of the initial $LiNiFeF_6$ phase were taken from our previous study[20]. The atomic coordinates of a newly formed Li-rich phase were derived from Rietveld refinement of the *ex situ* XRD analysis of the discharged cathode material. The microstructure parameters of all present phases were determined individually and were constantly refined over the entire period of the *in situ* experiment. Isotropic size-strain parameters were used for the initial Li-poor phase.

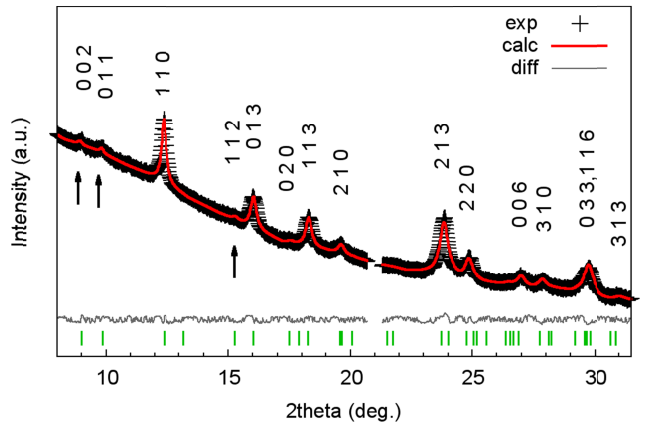

Figure 2. X-ray powder diffraction pattern and Rietveld refinement results of the ball-milled $LiNiFeF_6$/carbon/binder composite. Vertical lines at the bottom of the figure mark the positions of reflections of $LiNiFeF_6$. Characteristic "trirutile" superstructure reflections *hkl* with *l*≠3*n* are indicated by arrows.

For the Li-rich phase, the phenomenological model of anisotropic peak broadening by Stephens[32] was used, because the isotropic size-strain model cannot account for the observed peak broadening effects in the powder diffraction data.

2.2. *Ex situ* X-ray characterisation

In addition to *in situ* XRD characterisation, an $LiNiFeF_6$ cathode containing 15.4 mg $LiNiFeF_6$ active material was cycled at a current density of 5.69 mA g^{-1} (~ C/20) in a two-electrode Swagelok-type cell to the discharged state at 2.0 V (x = 0.85 Li per formula unit $Li_{1+x}NiFeF_6$). The sample was sealed by polyimide foil, including the aluminium current collector and the separator, and 20 diffraction images were recorded with an exposure time of 30 sec. The images were integrated for performing the Rietveld analysis.

2.3. ^{7}Li NMR

^{7}Li magic-angle spinning (MAS) nuclear magnetic resonance (NMR) spectroscopy was performed using a Bruker Avance 200 MHz spectrometer (B_0 = 4.7 T) with 2.5 mm zirconia rotors. An aqueous 1 M LiCl solution was used as a reference for the chemical shift of ^{7}Li (0 ppm). The values for the recycle delay and the π/s pulse length were 1 s and 2 µs, respectively. All NMR experiments were performed at room temperature (298 K) with a spinning speed of 30 kHz, and a rotor-synchronised Hahn-echo sequence (π/2–τ–π–τ–acquisition).

2.4. *In operando* XAS

In operando XAS measurements were performed at the µSpot beamline of the BESSY II synchrotron light source, Berlin, Germany. A cathode containing 15.2 mg $LiNiFeF_6$ active material was cycled against the lithium metal anode under galvanostatic conditions with a current density of 3.796 mA g^{-1}

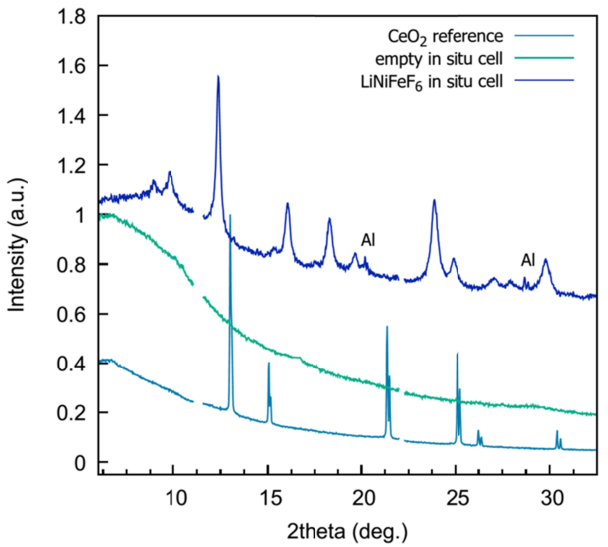

Figure 3. X-ray diffraction pattern of the $LiNiFeF_6$ *in situ* cell and the contributions of cell components without electrode film together with the diffraction pattern of CeO_2 reference powder.

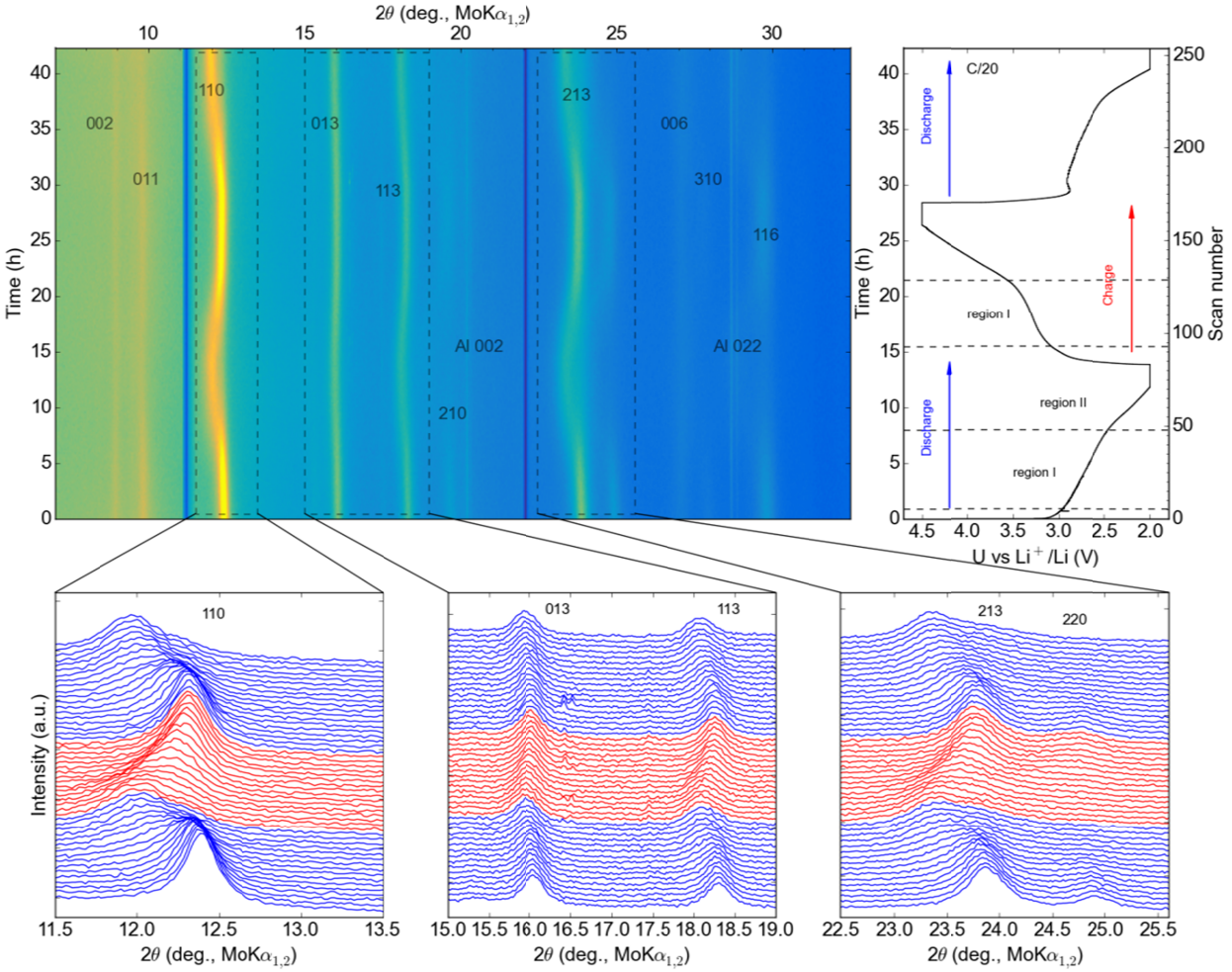

Figure 4. Contour plot and selected enlarged views of the *in situ* X-ray diffraction data showing the evolution of reflection positions and intensities as a function of cycling time and cell potential over the entire duration of the experiment.

(~C/30). The special cell described above was provided with an additional steel enclosure for better handling. First, XAS spectra were collected in the initial state. Then, the cell was connected to the potentiostat and cycled to potential steps of 2.8, 2.0, 3.5, and 4.5 V for the *in operando* spectroscopic measurements. Subsequently, the cell was fixed to the sample holder and XAS spectra were recorded in the transmission mode at the Ni and Fe K-edges. Absolute energy calibration of the monochromator was carried out by measuring a reference foil of pure Ni or Fe simultaneously with the cell. Gas-filled ionisation chambers were used to record the intensities of the incident beam and beams transmitted through the cell and the reference foil. In addition, various Ni- or Fe-containing reference compounds, such as NiF_2, FeF_2, and FeF_3, were also measured. The obtained data were aligned, normalised, and the background was subtracted as described elsewhere[33] using the ATHENA programme of the DEMETER software package[34]. As the different electrochemical charge/discharge states were attained, the cell was held at constant voltage to let the current decay and to move closer towards the thermodynamic equilibrium.

3. Results and discussion

As demonstrated in a previous work, the initial crystal structure of $LiNiFeF_6$ active material represents a partly ordered trirutile type[20] as displayed in Fig. 1. The structure with space group $P4_2/mnm$ and Z=2 can be derived from a stacking of three rutile unit cells, provided that at least two cations have a different ionic charge[35]. The F-anions form a slightly distorted hexagonal close packed lattice, in which Li^+, Mn^{2+}, and Fe^{3+} ions are in octahedral coordination, occupying the 2a site and a 4e site among edge-sharing [001]-chains. A preferred ordering in the cation arrangement is reflected by the appearance of additional superstructure reflections *hkl* with *l≠3n* in the diffraction pattern (e.g. *002*, *011*, or *112*) as can be seen in Fig. 2. Their intensity is determined by the difference in atomic scattering factors of cations occupying the 2a and 4e sites and varies with the magnitude of cation

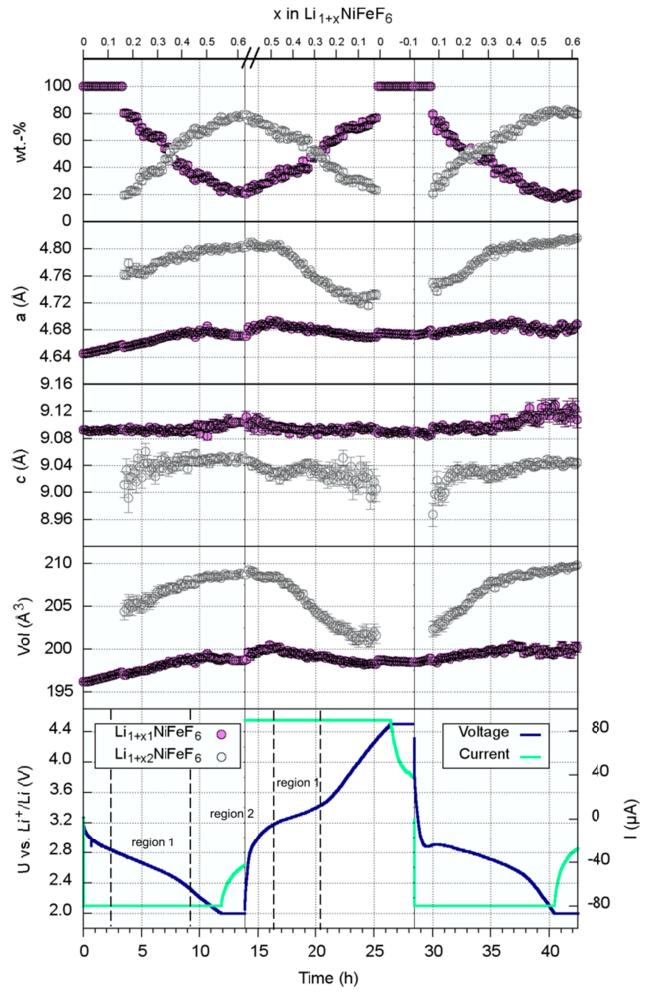

Figure 5. Results from Rietveld refinement showing the evolution of weight fractions and unit cell parameters of the Li-poor $Li_{1+x1}NiFeF_6$ and Li-rich $Li_{1+x2}NiFeF_6$ trirutile phase upon lithium insertion and extraction throughout the *in situ* experiment.

ordering. The degree of ordering depends on the synthesis method. In the as-synthesised $LiNiFeF_6$ lithium ions predominantly occupy the 2a position, while Ni and Fe are statistically distributed on the 4e site. A partial cation exchange between the two sites with a site occupation factor of the transition metals on the 2a site of approximately 23 % was estimated[20] (ideal ordering equals an exchange factor of 0 %). Due to similar atomic scattering factors, the sites of the two transition metals cannot be distinguished any further by X-ray diffraction. However, considering Pauling's fourth rule which states that cations with high valency and low coordination number tend not to share their coordinating polyhedra[36], an ordering of iron cations in every third layer is likely. The structure refinement of the processed $LiNiFeF_6$/carbon/binder composite (Table 1) shows an alteration of the atomic structure due to the applied ball-milling procedure that reduces the degree of ordering to a final cation exchange factor of 36 % between Li and transition metals. High-energy ball milling applied by Liao et al.[21] to obtain crystalline $LiFeFeF_6$ and $LiMgFeF_6$ even led to a completely random order among the cation chains.

The apparent crystallite size and micro strain parameter of the as-synthesised $LiNiFeF_6$ were determined to be 47(4) nm and 7.9(4) × 10^{-4}, respectively, in the previous study[20]. The ball-milled sample used as cathode material for *in situ* experimentation had an average micro strain parameter of 2.55(4) × 10^{-3} and an apparent crystallite size of 27(1) nm.

3.1. X-ray diffraction of the *in situ* battery

Fig. 3 displays the diffraction patterns of the $LiNiFeF_6$ *in situ* cell, the contributions of the regular cell components without electrode film as well as the diffraction pattern of an annealed CeO_2 powder glued between two polyimide foils for detector calibration. Narrow gaps in the diffraction patterns originate from gaps between the detector modules of the Pilatus 300K-W detector. The full width at half maximum (FWHM) of the CeO_2 reference sample is approximately constant (2θ = 0.06°) over the 2θ range from 10 to 32°. A splitting of the diffraction peaks due to the Mo-K$\alpha_{1,2}$ radiation is evident in CeO_2 at diffraction angles of 15° and higher. The high background level, especially at low 2θ values, is caused by amorphous cell components, such as the polyimide windows, glass fibre separator, and electrolyte, which are penetrated by the incident X-ray beam. All these components cause absorption of the primary and diffracted beams. Sharp reflections by the

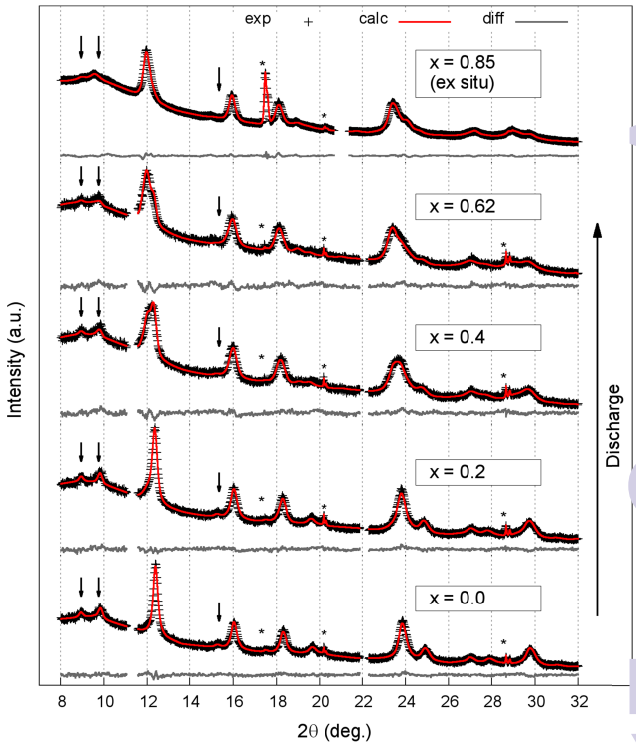

Figure 6. a) Selected XRD patterns (black) and Rietveld refinement results (red) showing the phase evolution in various states of the redox process. An *hkl*-dependent reflection shift and peak broadening upon electrochemical cycling can be observed. With progressive discharging, the trirutile superstructure reflections (marked by arrows) become noticeably weaker. Asterisks mark the positions of reflections by the Al current collector.

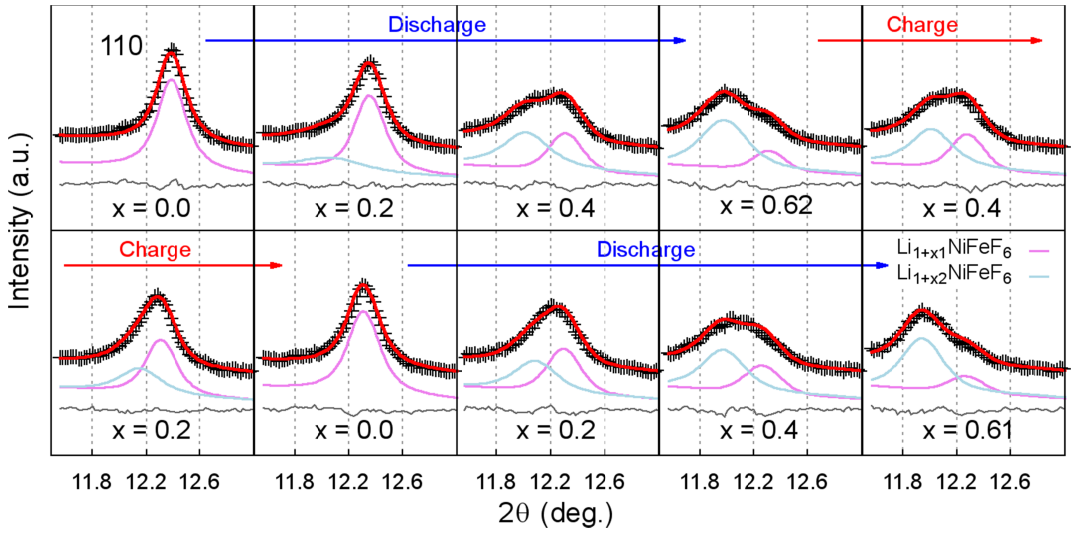

Figure 7. XRD patterns (black) and Rietveld refinement results (red) of the selected 2θ region displaying the shift and broadening of the *110* reflection upon electrochemical cycling and the contributions of Li-poor $Li_{1+x1}NiFeF_6$ and Li-rich $Li_{1+x2}NiFeF_6$.

Al current collector can be seen at 2θ = 20.2° and 2θ = 28.7°.

3.2. *In situ* XRD

Cycling of the $LiNiFeF_6$/Li cell was performed between 2.0 V and 4.5 V under constant current conditions with a rate of C/20. It started with discharging from an initially open circuit voltage of ~ 3.27 V. At the end of each discharge and charge half-cycle, the cell was held at the constant cut-off voltage for 2 hours in order to allow for the relaxation and thermodynamic equilibrium of the electrode material. Fig. 4 displays a contour plot of the diffracted intensities during the whole *in situ* experiment in the 2θ region between 7° and 32.5°, together with the electrochemical data on the right and enlarged views of the diffraction patterns at the bottom. They illustrate the observed phase transformations during cell operation. The recorded voltage signal shows regions with reduced slope, corresponding to regions of increased capacity (region I) and regions with higher slope (region II). Region I is found between 2.8 and 2.3 V in discharge and between 3.2 and 3.4 V during charge.

Comparison with previously published electrochemical data of $LiNiFeF_6$ by Lieser et al.[20] confirms the reliability of the *in situ* cell. According to slow scan cyclic voltammetry measurements, the maximum discharge current is located at 2.97 V, which is slightly higher than the region I in Fig. 4. The highest charge current is detected at 3.24 V, which is in good agreement with the data of the *in situ* cell. The higher electrode polarisation during discharging is most likely related to a higher thickness of the cathode used for this measurement and a smaller pressure force in the *in situ* cell. Similar to the results of the previous electrochemical study by Lieser et al.[20], an increase in discharge potential after the first discharge cycle can be observed for the *in situ* cell.

The overall discharge capacity is 70.5 and 69.7 mAh g^{-1} in the first and second discharge cycle, respectively, corresponding to an insertion of 0.62 and 0.61 mole lithium per formula unit. The charge cycle provides for a higher capacity of 82.8 mAh g^{-1}, which likely results from the combination of the electrochemical reaction in the cathode material with the oxidation of the electrolyte in the high-voltage region. An extraction of more than one mole lithium per formula unit is not expected based on the results of our previous study[20]. Considering the large thickness of the cathode, which is not ideal from an electrochemical point of view, but necessary for sufficient interaction with the incident X-ray beam, the achieved specific capacity of the *in situ* cell is in an adequate range.

The evolution of the diffraction patterns in Fig. 4 reflects the stability of the trirutile structure over the whole process of insertion and extraction, which is consistent with the findings from *ex situ* XRD of $LiNiFeF_6$[20] and *in situ* XRD of isostructural $LiFeFeF_6$[21]. The diffraction patterns show an *hkl*-dependent 2θ shift to smaller diffraction angles during discharging (lithium insertion) and a reversible shift upon charging (lithium extraction). Particularly the reflections with indices $h,k \neq 0$, such as *110*, *113*, and *213*, exhibit a significant shift, whereas the positions of the reflections with $h = k = 0$ and $l \neq 0$, such as *002* and *006*, do not change noticeably. While the discharge voltage passes the region from 2.6 to 2.0 V vs. Li^+/Li^0, several reflections develop a significant line broadening until the end of the discharge cycle. During the subsequent charge cycle, the FWHM of the diffraction peaks decreases again and reaches almost the initial values, demonstrating the good reversibility of the electrochemical reaction.

Based on these findings, a single phase model was used for the early stages of the discharge process (0 < x < 0.16 in $Li_{1+x}NiFeF_6$), whereas a two-phase model was employed in the Rietveld refinements for the later stages. We use x to denote the excess lithium of $Li_{1+x}NiFeF_6$ relative to the total amount of active material present. In the two-phase region we distinguish between the two Fe^{3+}/Fe^{2+} mixed-valent intermediate Li-poor $Li_{1+x1}NiFeF_6$ and Li-rich $Li_{1+x2}NiFeF_6$ phases, where $x1 \lesssim 0.16$

Table 1. Rietveld refinement results of atom coordinates in initial ball-milled $LiNiFeF_6$ (R_{wp} = 2.71 %) and discharged Li-rich $Li_{1+x2}NiFeF_6$ (R_{wp} = 3.20 %) determined by *ex situ* XRD. On the basis of Rietveld refinement results of fluorine positions and the results from ^{7}Li NMR, the intercalated lithium (Li3) is supposed to be accommodated on a 4c site in the discharged state.

Sample	Atom	Site	x	y	z	occ
Initial	Li 1	2a	0	0	0	0.64(1)
	Li 2	4e	0	0	0.3296(16)	0.18(1)
	Ni/Fe 1	2a	0	0	0	0.36(1)
	Ni/Fe 2	4e	0	0	0.3296(16)	0.82(1)
	F 1	4f	0.3101(17)	0.3101(17)	0	1
	F 2	8j	0.2930(16)	0.2930(16)	0.3274(18)	1
Discharged (*ex situ*)	Li 1	2a	0	0	0	0.29(1)
	Li 2	4e	0	0	0.3172(4)	0.36(1)
	Li 3 (theor.)	4c	0	0.5	0	0.345*
	Ni/Fe 1	2a	0	0	0	0.71(1)
	Ni/Fe 2	4e	0	0	0.3172(4)	0.65(1)
	F 1	4f	0.2774(24)	0.2774(24)	0	1
	F 2	8j	0.3079(12)	0.3079(12)	0.3124(10)	1

* Assuming an insertion of up to 0.16 eq. lithium into Li-poor $Li_{1+x1}NiFeF_6$ as indicated by *in situ* XRD results.

and x2 ≳ 0.16.

The results of the Rietveld refinements, i.e. the change of the lattice parameters and the evolution of the weight fractions during discharge and charge, are displayed in Fig. 5. Selected diffraction patterns taken at different states of the redox process, together with the calculated patterns, are displayed in Fig. 6. At the beginning of the discharge process (x = 0 - 0.16 in $Li_{1+x}NiFeF_6$), the electrochemical reaction proceeds via a single trirutile phase, similar to a solid-solution mechanism which is also reflected by a strongly sloping voltage curve. The *a*-lattice parameter increases slightly, while lattice parameter *c* remains almost constant. When a lithium content of x = 0.16 is exceeded (near 2.8 V), the cell potential loses slope and transitions into region I. The appearance of a shoulder on the low angle side of the reflections can then be observed. This asymmetry is most distinct at Bragg reflections with *h,k ≠ 0*, such as *110* (displayed in Fig. 7), *113*, and *213*. The appearance of additional Bragg intensity on the low angle side of the diffractions peaks indicates a phase separation and the beginning of a two-phase reaction between a lithium-poor phase $Li_{1+x1}NiFeF_6$ and a lithium-rich phase $Li_{1+x2}NiFeF_6$, both with trirutile structure. Further insertion of lithium results in an increase of the weight fraction of the newly formed $Li_{1+x2}NiFeF_6$ phase and a decrease of the $Li_{1+x1}NiFeF_6$ phase. At the same time, the Bragg positions of the Li-rich $Li_{1+x2}NiFeF_6$ phase shift towards lower 2θ values. For 0.17 < x < 0.4, a change in the *a*-lattice parameters of both the initial $Li_{1+x1}NiFeF_6$ and the $Li_{1+x2}NiFeF_6$ can be observed. The larger unit cell volume of the $Li_{1+x2}NiFeF_6$ phase suggests an increased capability of Li uptake upon this biphasic reaction. As region I between 2.8 and 2.3 V is passed, the weight fraction of $Li_{1+x2}NiFeF_6$ increases steadily and the unit cell volumes of both phases show further expansion. At a discharge potential of 2.51 V (x = 0.35 in $Li_{1+x}NiFeF_6$), half of the initial phase has been transformed into the new Li-rich trirutile phase.

It must be noted that the volume expansion during discharge is solely induced by an increase in the *a*-lattice parameter. The *c*-lattice parameter stays nearly constant for both phases, except for the beginning of the two-phase regime, where the refined *c*-lattice parameter of the $Li_{1+x2}NiFeF_6$ phase exhibits significant scattering with relatively high errors due to the low weight fraction existing in this state. As the lithium content exceeds a value of 0.4, the lattice metrics of the two phases exhibits a different behaviour. In contrast to the Li-rich $Li_{1+x2}NiFeF_6$ phase, where the *a*-lattice parameter increases further, the *a*-lattice parameter of the Li-poor $Li_{1+x1}NiFeF_6$ phase remains nearly constant. Until the cut-off voltage of 2.0 V is reached, the amount of inserted lithium increases further up to x = 0.55 per formula unit and a fraction of ~ 74 wt.-% of the Li-rich $Li_{1+x2}NiFeF_6$ phase is achieved. During the constant voltage step of two hours at 2.0 V, the current decreases exponentially and the phase transformation continues, while the cathode material moves towards the thermodynamic equilibrium. At the end of the discharge cycle, an overall uptake of 0.62 Li per formula unit has been accomplished. The lattice parameters of the $Li_{1+x2}NiFeF_6$ phase are *a* = 4.8028(11) Å, *c* = 9.0501(35) Å and *a* = 4.6711(21) Å, *c* = 9.1040(71) Å for the $Li_{1+x1}NiFeF_6$ phase, with their weight fractions being 79 wt.-% and 21 wt.-%, respectively. The resulting unit cell volume amounts to 208.8(1) Å^3 and 198.6(1) Å^3 for $Li_{1+x2}NiFeF_6$ and $Li_{1+x1}NiFeF_6$, respectively, which is an increase of ~ 6.4 % and ~ 1.2 % compared to the initial unit cell volume. This volume expansion is of the same order of magnitude as those of commercially cathode materials, such as spinel-type $LiMn_2O_4$ (6.4 – 6.5 %[37,38]) or olivine-type $LiFePO_4$ (6.9 – 7.0 %[39,40]).

The charge cycle and the associated extraction of lithium start with a fast increase of the cell potential up to ~ 2.9 V. When region I is reached, the phase transitions are reversed. The weight fraction of the Li-poor $Li_{1+x1}NiFeF_6$ phase continuously increases, whereas the amount of the Li-rich $Li_{1+x2}NiFeF_6$ phase decreases. This phase transition is accompanied by a change of the lattice metrics of both phases, the changes in the $Li_{1+x2}NiFeF_6$ phase being significantly larger than in the $Li_{1+x1}NiFeF_6$ phase. The tetragonal *a*-lattice parameters of both phases decrease again until a composition of x = 0.15 is reached. From here on, the lattice metrics stays approximately

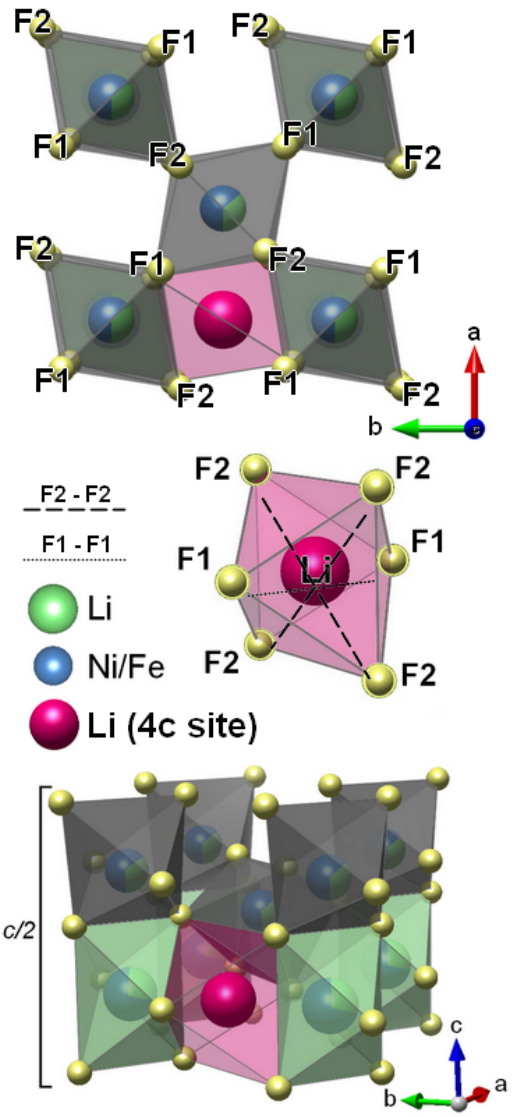

Figure 8. Schematic model of Li insertion into the tritutile channels on the octahedral 4c site of the discharged Li-rich $Li_{1+x2}NiFeF_6$.

constant (apart from the c-lattice parameter of the Li-rich phase with a high uncertainty at very small weight fractions). The limit of the co-existence region of the two phases is reached at 4.29 V. The diffraction patterns can be attributed again to a single tritutile structure with $Li_{1+x}NiFeF_6$ compositions reaching x = 0. The change in the reaction mechanism to a pure solid-solution behaviour is also reflected by an increase of the slope of the charge voltage profile at about 3.6 V. The lattice parameters and the unit cell volume at the end of charge are a = 4.6736(4) Å, c = 9.0873(16) Å, and V = 198.5(1) $Å^3$, respectively. The amount of extracted lithium calculated from the charge current is 0.67 mole per formula unit at the beginning of the 4.5 V voltage step and increases up to 0.73 mole during the potentiostatic step. This state of charge exceeds the amount of lithium ions that had been inserted during the discharge cycle (0.62 Li per formula unit). Our previous study[20] showed that lithium extraction from $LiNiFeF_6$ is not possible up to 4.5 V. Hence, the excess current may originate from electrolyte decomposition. The phase transition behaviour during the second discharge cycle is nearly identical to that of the first discharge cycle, thus demonstrating the reversibility of the (de-)insertion of lithium into the tritutile host structure. Nevertheless, a slightly higher discharge voltage can be noticed. The small deviation from initial lattice parameters and increase in unit cell volume of ~ 1% after the charge cycle may affect the electrical resistance of the host structure and enhance lithium diffusivity.

The observed phase separation mechanism, where not only the weight fractions, but also the lattice parameters of the reacting phases change, is rather unexpected. Recently, such two-phase reactions with a simultaneous evolution of the lattice metrics were also reported for the $LiVPO_4O$-VPO_4O[41], the $NaFePO_4$-$FePO_4$[42], and the FeOF systems[43]. Many research groups[44] investigated a similar phenomenon in lithium metal phosphate. It was found that in a partly transformed material, where two-phase particles may exist, elastic strain caused by lattice mismatch can affect thermodynamic and kinetic aspects of the phase transition[45]. A barrier to nucleation of the second phase and its growth through interface motion has to be overcome and sometimes, a deviation from the equilibrium processes is possible. It produces metastable and transient nonstoichiometric phases which lead to gradual shifts of Bragg reflections even in the apparent two-phase reaction range[46]. It was shown that the solubility limits of the phase-separating phases increase with decreasing particle size[47]. This is highly evident for nanoscaled active material with a particle size similar to that of the $LiNiFeF_6$ considered here. Apparently, the transient region of phase transformation in $Li_{1+x}NiFeF_6$ is completed as x = 0.4 is exceeded. The stabilisation of the *a* lattice parameter of the Li-poor phase suggests that this phase does not take up any further excess lithium. Furthermore, a decrease in the two-phase reaction rate can be observed. A predominant solid-solution behaviour of the Li-rich $Li_{1+x2}NiFeF_6$ phase towards the end of the discharge cycle is also reflected by a significant increase in the slope of the potential curve.

3.3. Lithium insertion into tritutile channels

According to the results of *in situ* X-ray diffraction, a preservation of the tritutile host structure can be assumed and the lithium insertion mechanism can be considered an insertion process. Inserted lithium cannot be detected by X-ray diffraction due to its low scattering power and the presence of the heavy transition metals. Nevertheless, observations of the

Table 2. Rietveld refinement results of the fluorine distances and octahedral volume of the 4c site in the discharged state at 2.0 V providing possible insertion sites for additional lithium as displayed in Figure 8.

	Initial $LiNiFeF_6$	Discharged Li-rich $Li_{1+x2}NiFeF_6$ (*ex situ*)
F2-F2 (equatorial) [Å]	4.577(18)	4.863(11)
F1-F1 (axial) [Å]	3.378(12)	3.420(17)
V (oct.) [$Å^3$]	11.748	13.376

changes in interatomic distances of the host structure are helpful to investigate the insertion mechanism. The anisotropy in the lattice parameter changes suggests an insertion of lithium cations into the trirutile channels similar to the process observed in Li_xWO_2 and Li_xMoO_2[48], $LiFeFeF_6$[21], and the rutile structure of TiO_2[24]. In the trirutile structure the empty [001] channels are considered unidirectional lithium diffusion paths. However, in the initially charged state, the channels are very narrow regarding the ionic radius of Li^+ of approximately 0.74 Å[49] in octahedral coordination. Thus, an expansion of the channel width in the *a*-*b*-plane is likely to allow for the insertion of additional lithium.

In order to obtain deeper insights into the effects of lithium insertion on the crystal structure, an additional sample was cycled to the discharged state at 2.0 V (x = 0.85 Li per formula unit $Li_{1+x}NiFeF_6$) for *ex situ* XRD analysis with higher counting time, allowing for Rietveld refinement of atomic coordinates. Rietveld refinement (Fig. 6) reveals a phase fraction of ~ 21 wt.-% Li-poor $Li_{1+x1}NiFeF_6$ and ~79 wt.-% Li-rich $Li_{1+x2}NiFeF_6$. The lattice parameters of the Li-rich phase are a = 4.8072(4) Å and c = 9.0305(9) Å, implying a slightly higher expansion in the *a*-*b*-plane compared to the results of *in situ* XRD which is consistent with the higher amount of inserted lithium. Furthermore, a change in atomic positions (Table 1) and an associated expansion of the trirutile channels can be detected.

Within the channels, the crystal structure provides an empty 4c site (0, ½, 0), allowing for lithium insertion into octahedral coordination as displayed in Fig. 8. Theoretically, there is also the possibility of lithium insertion in tetrahedral coordination. However, density-functional calculations for isomorphic rutile-Li_xTiO_2 by Koudriachova et al.[50] indicate an energetically favourable accommodation of lithium on the octahedral site. These vacant channel sites have also been suggested as lithium insertion sites in Li_xRuO_2[51] and Li_xMoO_2[52] with rutile structure. In this (0, ½, 0)-configuration the Li octahedra share two opposite faces and two opposite edges with adjacent octahedra. An expansion of the three diagonal F-F ion distances from the initial to the discharged state (Table 2) corroborates the assumption of Li insertion. Upon discharging, the octahedral volume of the 4c site increases by ~ 14 % from 11.75 Å^3 to 13.38 Å^3. Liao et al.[21] claimed that during the sloping of the charge/discharge voltage curve, lithium is not only (de-)inserted from/into the channels of $LiFeFeF_6$, but can also be extracted from its octahedral chains. They justified this suggestion by an observed peak broadening in the *013* and *113* reflections, which they attribute to a c-axis strain. However, the data presented in this study do not reflect this phenomenon.

Besides the changes in the distances between F ions, the refinement of the *ex situ*-measured Li-rich $Li_{x+x2}NiFeF_6$ structure provides evidence of further cation exchange between the 2a and 4e sites. The initially determined cation exchange factor between Li and transition metals of 36 ± 1 % increases to 71 ± 1 % (Table 1). Also, a deviation from the ideal trirutile arrangement is indicated by a decrease of the superstructure reflection intensities, as can be seen in Fig. 6. The changes in the oxidation state of Fe ions upon discharge

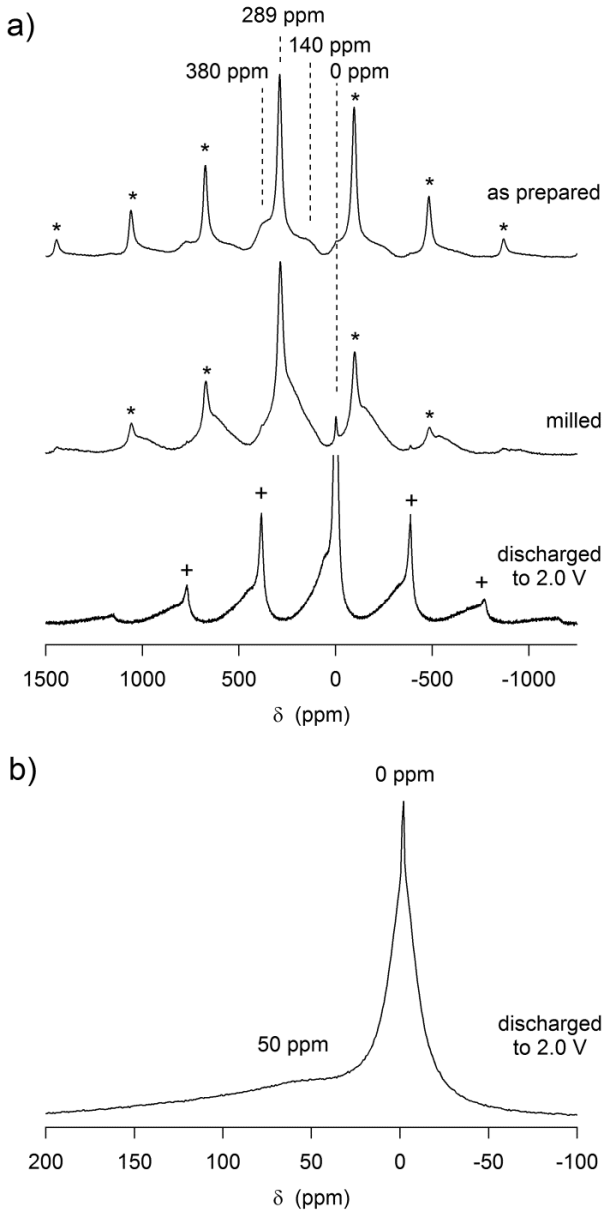

Figure 9. a) ^{7}Li MAS NMR spectra of $LiNiFeF_6$ directly after synthesis, after milling with PVdF and carbon, and after discharging against Li metal down to 2.0 V. Spinning sidebands are marked by an asterisk and a cross. b) Magnified view of the spectrum obtained after discharging to 2.0 V.

and the associated increase in ionic radius significantly contribute to the anisotropic expansion of the host structure. Rietveld refinement of the *ex situ*-measured Li-rich $Li_{1+x2}NiFeF_6$ phase indicates an increase of the octahedral volume of the 4e site by ~ 11 % and a significant axial elongation on the *a*-*b*-plane (Me-F_{axial} = 2.00 Å and Me-$F_{equitorial}$ = 2.10 Å). The metal-fluorine distances are in good agreement with Fe-F distances in FeF_2 known from literature (Fe-F_{axial} = 1.99 Å and Fe-$F_{equitorial}$ = 2.12 Å)[53]. The distortion can be associated with the Jahn-Teller effect which is known to be notably strong for Fe^{2+} in octahedral coordination[54]. A quantitative measure of the magnitude of the distortion is the octahedral distortion parameter Δd[55].

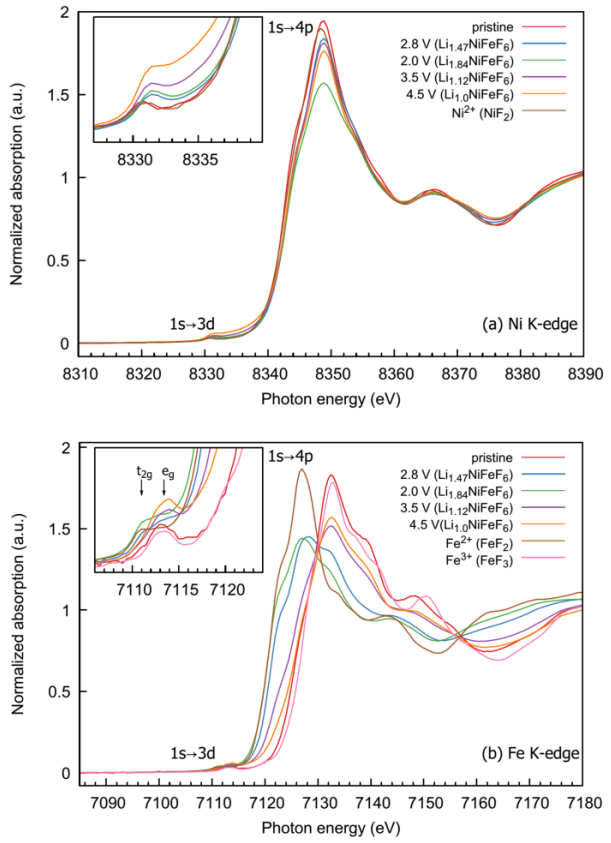

Figure 10. Normalized absorption spectra at the (a) Ni and (b) Fe K-edges of $Li_{1+x}NiFeF_6$ in various states of discharge and charge. The insets show expanded views of the pre-edge regions.

Octahedral distortion parameters $\Delta d_{initial} = 1.9 \times 10^{-4}$ and $\Delta d_{discharged} = 114.5 \times 10^{-4}$ are observed for the 4e site, whereas the distortion parameters $\Delta d_{initial} = 0.8 \times 10^{-4}$ and $\Delta d_{discharged} = 36.4 \times 10^{-4}$ of the 2a site are significantly smaller. The higher distortion of F-ligands around the 4e site implies the presence of reduced Fe^{2+} ions inducing this anisotropic expansion. Moessbauer spectra of $LiNiFeF_6$ after discharging to 2.0 V presented by Lieser et al.[20] confirm these findings and reflect a broad doublet with an isomer shift characteristic of Fe^{2+}. The spectrum suggests a distribution of electric field gradients at the Fe sites, indicating strong variations, i.e. distortions, in the local environment around these ions.

Contrary to the 4e site, Rietveld refinement shows that the octahedral 2a site actually exhibits a slight volume contraction upon discharge (~ 4 %), which is most likely due to the occupation of adjacent 4c positions by intercalated lithium.

3.4. ^{7}Li NMR

Fig. 9 shows the ^{7}Li MAS NMR spectra of $LiNiFeF_6$ directly after synthesis, after milling with PVdF binder and carbon, and after discharging in a battery cell against lithium metal down to 2.0 V. The spectrum of the sample obtained directly after synthesis is dominated by a strong narrow peak at 289 ppm, representing the Li ions on the regular 2a sites of the trirutile structure. The very large NMR shift is caused by the transfer of unpaired electron spin density from the transition metal ions (Fe^{3+} and Ni^{2+}) via F to the Li nucleus[56] and, thus, confirms the presence of Li-F-(Fe/Ni) bonds. Additional broader contributions are visible at about 380 and 140 ppm. These broad peaks may be caused by Li ions located on the 4e sites and also by the Fe/Ni cation disorder on the transition metal sites around the Li ions. Another possible explanation might be the presence of structural disorder in the surface regions of the small crystallites. After milling of the $LiNiFeF_6$ together with PVdF and carbon, a similar ^{7}Li NMR spectrum is obtained, but the broad components show further broadening revealing an increase in structural disorder, i.e. variations of the bond lengths/angles, most likely in the surface-near regions of the crystallites[57]. A small, narrow contribution at 0 ppm also reveals that milling induces the formation of a diamagnetic phase, probably a small amount of LiF. After discharging to 2.0 V, i.e. incorporation of about 0.9 additional Li per formula unit $LiNiFeF_6$ into the crystal structure, the original peaks in the spectrum disappear completely and two new, broad contributions with similar integral intensities are present at 50 ppm and 0 ppm (Fig. 9b). Two different effects cause these changes in the spectrum: firstly, the incorporation of lithium on initially empty sites causes the appearance of additional peaks. Secondly, the accompanying reduction of Fe^{3+} to Fe^{2+} changes the local environments of the already existing Li ions and, thus, causes strong shifts of the original peaks. The much smaller (positive) shifts observed after discharging to 2.0 V are in agreement with earlier observations of the contributions of Fe^{2+} to the overall NMR shifts being much smaller (or even negative) in comparison to Fe^{3+} [58,59]. The fact that the two new peaks are quite broad is in agreement with the variations in the Fe-F bond lengths as observed by XRD. On top of the broad contribution around 0 ppm, another narrower contribution is present, which suggests some residues of the electrolyte salt.

3.5. *In operando* XAS

The X-ray absorption near edge structure (XANES) measurements at the Ni and Fe K-edges of the $LiNiFeF_6$ cathode at various states of charge and discharge, together with the XANES spectra of some reference compounds, are shown in Fig. 10. These XAS measurements demonstrate the reversibility of the electrochemical redox reaction occurring in the course of lithiation and delithiation of the material. All K-edge spectra feature a pre-edge region which corresponds to the 1s→3d electric-dipole-forbidden, but quadrupole-allowed transition and a vertically rising main edge with a maximum corresponding to the 1s→4p transition[60]. The position of the 1s→4p peak at the Fe K-edge in the pristine $LiNiFeF_6$ cathode is very similar to that of the Fe^{3+}-containing FeF_3 reference material. As the cathode is discharged to 2.8 V (x = 0.47 in $Li_{1+x}NiFeF_6$), the Fe K-edge shifts to lower energies and lies between the edges of the Fe^{2+}- and Fe^{3+}-containing reference compounds FeF_2 and FeF_3. At 2.0 V, the Fe K-edge is very close to the edge of the FeF_2 reference. This voltage corresponds to a nominal composition of $Li_{1.84}NiFeF_6$ (the Li content in $Li_{1+x}NiFeF_6$ was calculated based on the measured capacity). As

the cell is charged to 3.5 V (x = 0.12 in $Li_{1+x}NiFeF_6$) and finally to 4.5 V (x = 0 in $Li_{1+x}NiFeF_6$), the 1s→4p peak moves back to its original position. In contrast to this, the Ni K-edges do not show any chemical shift. In the pristine state as well as in the different charged and discharged states the spectra are almost identical to those of the NiF_2 reference. The XANES region is mostly determined by valence, the symmetry of the local environment, and the nearest-neighbour bond length. These results confirm that only Fe^{3+} participates in the electrochemical process via an Fe^{3+}/Fe^{2+} redox reaction, while Ni^{2+} remains electrochemically inactive. A complete conversion of Fe^{3+} into Fe^{2+} during discharging of $LiNiFeF_6$ active material to 2.0 V was observed in a previous study[20] by Moessbauer spectroscopy. The presence of a small pre-edge feature, weak 1s→3d peaks at approximately 7113 eV and 8331 eV, in the Fe and Ni spectra (see insets of Fig. 10) indicates some asymmetry of the fluorine octahedra around the two transition metal ions.

4. Conclusions

The present study provides insights into the chemical and structural transformations taking place during the electrochemical cycling of $LiNiFeF_6$. *In situ* X-ray diffraction reveals an unexpected transient phase separation mechanism. Based on the evolution of the positions and profile shape of the reflections in the XRD patterns, a two-phase model is proposed for the lithium (de-)insertion processes. In addition, each of the two co-existing phases, Li-poor $Li_{1+x1}NiFeF_6$ and Li-rich $Li_{1+x2}NiFeF_6$ with x1 $\lesssim$ 0.16 and x2 $\gtrsim$ 0.16, exhibits an anisotropic change of lattice parameters. Up to an overall Li content of approximately x = 0.4 in $Li_{1+x}NiFeF_6$, an increase in the *a*-lattice parameters leads to a significant volume expansion of both phases, while the *c*-lattice parameters remain nearly constant. The Li-rich phase exhibits a strong anisotropic expansion in the *a*-*b*-plane, which is interpreted as being due to a high lithium uptake capability into [001] channels of the trirutile structure. Both the shape of the potential curve and the further evolution of lattice parameters indicate a termination of the transient region of phase reaction and a transformation to a predominantly solid-solution behaviour of the Li-rich $Li_{1+x2}NiFeF_6$ phase, as x exceeds 0.4 in $Li_{1+x}NiFeF_6$. Changes of atomic coordinates and bond distances determined by *ex situ* XRD suggest the accommodation of intercalated lithium on the empty six-fold coordinated 4c site. This is confirmed by ^{7}Li MAS NMR spectroscopy which shows two Li environments with similar intensities after discharging to 2.0 V. *In operando* XANES measurements suggest that Fe is the metal ion actively participating in the electrochemical redox reaction, whereas Ni shows no chemical shift at any state of charge. A distortion and anisotropic expansion of F-ligand bonds around the 4e site are observed due to variations in Fe ionic radii during the redox reaction.

Acknowledgements

The author wishes to thank the HZB for allocated beam time and their technical support.

Notes and references

1 B. Xu, D. Qian, Z. Wang, and Y. S. Meng, *Mater. Sci. Eng. R*, 2012, **73**, 51–65.

2 A. Kraytsberg and Y. Ein-Eli, *Adv. Energy Mater.*, 2012, **2**, 922–939.

3 Y. Koyama, I. Tanaka, and H. Adachi, *J. Electrochem. Soc.*, 2000, **147**, 3633–3636.

4 M. E. Arroyo y de Dompablo, U. Amador, and J. Tarascon, *J. Power Sources*, 2007, **174**, 1251–1257.

5 M. Schroeder, C. Eames, D. A. Tompsett, G. Lieser and M. S. Islam, *Phys. Chem. Chem. Phys.*, 2013, **15**, 20473–9.

6 T. T. Esaka, R. Okuyama, E. Chemistry, and I. S. Limmf, *Solid State Ionics*, 1989, **34**, 201–205.

7 M. Park, X. Zhang, M. Chung, G. B. Less, and A. M. Sastry, *J. Power Sources*, 2010, **195**, 7904–7929.

8 F. Badway, F. Cosandey, N. Pereira, and G. G. Amatucci, *J. Electrochem. Soc.*, 2003, **150**, A1318–A1327.

9 E. Gonzalo, A. Kuhn, and F. García-Alvarado, *J. Electrochem. Soc.*, 2010, **157**, A1002–A1006.

10 A. Basa, E. Gonzalo, A. Kuhn, and F. García-Alvarado, *J. Power Sources*, 2012, **197**, 260–266.

11 M. Herklotz, F. Scheiba, M. Hinterstein, K. Nikolowski, M. Knapp, A.-C. Dippel, L. Giebeler, J. Eckert, and H. Ehrenberg, *J. Appl. Crystallogr.*, 2013, **46**, 1117–1127.

12 M. Yavuz, N. Kiziltas-Yavuz, A. Bhaskar, M. Scheuermann, S. Indris, F. Fauth, M. Knapp, and H. Ehrenberg, *Zeitschrift für Anorg. und Allg. Chemie*, 2014, **640**, 3118–3126.

13 H. Li, P. Balaya, and J. Maier, *J. Electrochem. Soc.*, 2004, **151**, A1878–A1885.

14 I. D. Gocheva, T. Doi, S. Okada, and J. Yamaki, *Electrochemistry*, 2010, **78**, 471–474.

15 A. Basa, E. Gonzalo, A. Kuhn, and F. García-Alvarado, *J. Power Sources*, 2012, **207**, 160–165.

16 J. Kohl, D. Wiedemann, S. Nakhal, P. Bottke, N. Ferro, T. Bredow, E. Kemnitz, M. Wilkening, P. Heitjans, and M. Lerch, *J. Mater. Chem.*, 2012, **22**, 15819–15827.

17 N. Twu, X. Li, C. Moore, and G. Ceder, *J. Electrochem. Soc.*, 2013, **160**, A1944–A1951.

18 G. Lieser, M. Schroeder, H. Geßwein, V. Winkler, S. Glatthaar, M. Yavuz, and J. R. Binder, *J. Sol-Gel Sci. Technol.*, 2014, **71**, 50–59.

19 G. Lieser, L. de Biasi, M. Scheuermann, V. Winkler, S. Eisenhardt, S. Glatthaar, S. Indris, H. Geßwein, M. J. Hoffmann, H. Ehrenberg, and J. R. Binder, *J. Electrochem. Soc.*, 2015, **162**, A679–A686.

20 G. Lieser, C. Dräger, M. Schroeder, S. Indris, L. de Biasi, H. Geßwein, S. Glatthaar, H. Ehrenberg, and J. R. Binder, *J. Electrochem. Soc.*, 2014, **161**, A1071–A1077.

21 P. Liao, J. Li, and J. R. Dahn, *J. Electrochem. Soc.*, 2010, **157**, A355–A361.

22 G. Lieser, L. de Biasi, H. Geßwein, S. Indris, C. Dräger, M. Schroeder, S. Glatthaar, H. Ehrenberg, and J. R. Binder, *J. Electrochem. Soc.*, 2014, **161**, A1869–A1876.

23 G. Lieser, C. Dräger, L. de Biasi, S. Indris, H. Geßwein, S. Glatthaar, M. J. Hoffmann, H. Ehrenberg, and J. R. Binder, *J. Power Sources*, 2015, **274**, 1200–1207.

24 B. Zachau-Christiansen, K. West, T. Jacobsen, and S. Atlung, *Solid State Ionics*, 1988, **28-30**, 1176–1182.

25 W. De Nolf and K. Janssens, *Surf. Interface Anal.*, 2010, **42**, 411–418.

26 W. De Nolf, F. Vanmeert, and K. Janssens, *J. Appl. Crystallogr.*, 2014, **47**, 1107–1117.

27 P. Thompson, D. E. Cox, and J. B. Hastings, *J. Appl. Crystallogr.*, 1987, **20**, 79–83.

28 D. Balzar and H. Ledbetter, *J. Appl. Crystallogr.*, 1993, **26**, 97–103.

29 D. Balzar, N. Audebrand, M. R. Daymond, a. Fitch, a. Hewat, J. I. Langford, a. Le Bail, D. Louër, O. Masson, C. N. McCowan, N. C. Popa, P. W. Stephens, and B. H. Toby, *J. Appl. Crystallogr.*, 2004, **37**, 911–924.

30 P. Norby, *J. Appl. Crystallogr.*, 1997, **30**, 21–30.

31 K. Momma and F. Izumi, *J. Appl. Crystallogr.*, 2011, **44**, 1272–1276.

32 P. W. Stephens, *J. Appl. Crystallogr.*, 1999, **32**, 281–289.

33 S. D. Kelly, D. Hesterberg, and B. Ravel, in *Methods of Soil Analysis Part 5—Mineralogical Methods*, 2008, pp. 387–464.

34 B. Ravel and M. Newville, *J. Synchrotron Radiat.*, 2005, **12**, 537–41.

35 W. Viebahn, Habil., Universität Tübingen, 1976.

36 L. Pauling, *J. Am. Chem. Soc.*, 1929, **51**, 1010–1026.

37 X. Q. Yang, Sun, S. J. Lee, J. Mcbreen, S. Mukerjee, M. L. Daroux, and X. K. Xing, *Electrochem. Solid-State Lett.*, 1999, **2**, 157–160.

38 J. Christensen and J. Newman, *J. Electrochem. Soc.*, 2006, **153**, A1019.

39 D. Wang, X. Wu, Z. Wang, and L. Chen, *J. Power Sources*, 2005, **140**, 125–128.

40 A. K. Padhi, K. S. Nanjundaswamy, and J. B. Goodenough, *J. Electrochem. Soc.*, 1997, **144**, 1188–1194.

41 M. Bianchini, J. M. Ateba-Mba, P. Dagault, E. Bogdan, D. Carlier, E. Suard, C. Masquelier, and L. Croguennec, *J. Mater. Chem. A*, 2014, **2**, 10182.

42 M. Casas-Cabanas, V. V. Roddatis, D. Saurel, P. Kubiak, J. Carretero-González, V. Palomares, P. Serras, and T. Rojo, *J. Mater. Chem.*, 2012, **22**, 17421.

43 K. M. Wiaderek, O. J. Borkiewicz, E. Castillo-mart, R. Robert, N Pereira, G. G. Amatucci, C. P. Grey, P. J. Chupas, and K. W. Chapman, *J. Am. Chem. Soc.*, 2013, **135**, 4070–4078.

44 D. Li and H. Zhou, *Mater. Today*, 2014, **17**, 451–463.

45 N. Meethong, H.-Y. S. Huang, S. a. Speakman, W. C. Carter, and Y.-M. Chiang, *Adv. Funct. Mater.*, 2007, **17**, 1115–1123.

46 Y. Orikasa, T. Maeda, Y. Koyama, H. Murayama, K. Fukuda, H. Tanida, H. Arai, E. Matsubara, Y. Uchimoto, and Z. Ogumi, *Chem. Mater.*, 2013, **25**, 1032–1039.

47 N. Meethong, Y. Kao, M. Tang, H. Huang, W. C. Carter, and Y. Chiang, *Chem. Mater.*, 2008, **20**, 6189–6198.

48 D. B. Rogers, R. D. Shannon, A. W. Sleight, and J. L. Gillson, *Inorg. Chem.*, 1969, **8**, 841–849.

49 R. D. Shannon and C. T. Prewitt, *Acta Crystallogr. Sect. B Struct. Crystallogr. Cryst. Chem.*, 1969, **25**, 925–946.

50 M. Koudriachova, N. Harrison, and S. de Leeuw, *Phys. Rev. B*, 2002, **65**, 235423.

51 J. J. Davidson and J. E. Greedan, *J. Solid State Chem.*, 1984, **51**, 104–117.

52 D. E. Cox, R. J. Cava, D. B. McWhan, and D. W. Murphy, *J. Phys. Chem. Solids*, 1982, **43**, 657–666.

53 R. Boca, *Chem. Zvesti*, 1981, **35**, 769–777.

54 H. Brokopf, D. Reinen, and O. Schmitz-DuMont, *Zeitschrift für Phys. Chemie Neue Folge*, 1969, **68**, 228–241.

55 M. W. Lufaso and P. M. Woodward, *Acta Crystallogr. B.*, 2004, **60**, 10–20.

56 C. P. Grey and N. Dupré, *Chem. Rev.*, 2004, **104**, 4493–512.

57 S. Indris, M. Scheuermann, S. M. Becker, V. Šepelák, R. Kruk, J. Suffner, F. Gyger, C. Feldmann, A. S. Ulrich, and H. Hahn, *J. Phys. Chem. C*, 2011, **115**, 6433–6437.

58 R. Chen, R. Heinzmann, S. Mangold, V. S. K. Chakravadhanula, H. Hahn, and S. Indris, *J. Phys. Chem. C*, 2013, **117**, 884–893.

59 I. Bezza, M. Kaus, R. Heinzmann, M. Yavuz, M. Knapp, S. Mangold, S. Doyle, C. P. Grey, H. Ehrenberg, S. Indris, and I. Saadoune, 2015, submitted.

60 T. Yamamoto, *X-Ray Spectrom.*, 2008, **37**, 572–584.